Letter

Rydberg-ion flywheel for quantum work storage

Wilson S. Martins,[1] Federico Carollo,[1] Weibin Li,[2] Kay Brandner,[2] and Igor Lesanovsky[1,2]
[1]*Institut für Theoretische Physik, Universität Tübingen, Auf der Morgenstelle 14, 72076 Tübingen, Germany*
[2]*School of Physics and Astronomy and Centre for the Mathematics and Theoretical Physics of Quantum Non-Equilibrium Systems, The University of Nottingham, Nottingham NG7 2RD, United Kingdom*

(Received 20 April 2023; accepted 13 October 2023; published 6 November 2023)

Trapped ions provide a platform for quantum technologies that offers long coherence times and high degrees of scalability and controllability. Here, we use this platform to develop a realistic model of a thermal device consisting of two laser-driven, strongly coupled Rydberg ions in a harmonic trap. We show that the translational degrees of freedom of this system can be utilized as a flywheel storing the work output that is generated by a cyclic thermodynamic process applied to its electronic degrees of freedom. Mimicking such a process through periodic variations of external control parameters, we use a mean-field approach underpinned by numerical and analytical calculations to identify relevant physical processes and to determine the charging rate of the flywheel. Our work paves the way for the design of microscopic thermal machines based on Rydberg ions that can be equipped with both many-body working media and universal work storages.

DOI: 10.1103/PhysRevA.108.L050201

Introduction. Developing new types of thermal machines that generate useful work at small length scales is a central topic in stochastic and quantum thermodynamics [1–6]. Over the last decade, this area has seen remarkable progress driven by landmark experiments, in which thermodynamic engine cycles were realized with microscopic objects such as single ions [7–9], nuclear spins [10], nitrogen-vacancy centers in diamonds [11] or large quasispin states of ultracold atoms [12]. Practical applications of such devices are, however, still limited, with two problems currently emerging as key challenges: First, scaling up the power of microscopic thermal machines without losing access to genuine features stemming from quantum effects [13–35]; second, identifying viable strategies to transfer the generated output to universal storage systems, which can be accessed by other devices [7–9,23,36–38].

A promising approach to the first challenge is to replace working media with few degrees of freedom, such as single spins, with many-body systems, where collective effects can arise from the co-action of large numbers of constituents [13]. Recent theoretical and experimental studies have shown that the power of thermal devices can be significantly enhanced by exploiting, for example, many-body coherence in non-interacting systems, which can give rise to super-radiance and related phenomena [14–24], or interactions and quantum many-body statistics in ultracold atomic systems [25–35]. Strongly interacting Rydberg atoms and ions provide another, yet relatively unexplored, platform to implement quantum thermal machines with many degrees of freedom [39]. These systems show a rich phenomenology and can be realized in experiments with a high degree of control and access to internal state variables [40–42]. Rydberg ions, in particular, offer state-dependent interaction together with long-time stability [43–46].

In addition, interactions among Rydberg states give rise to an accurately controllable coupling between translational and internal electronic degrees of freedom [47,48]. This feature can be exploited to approach the second challenge in the development of practically applicable quantum thermal machines. Inspired by earlier experiments with single-body systems [7,8], the key idea here is to perform an engine cycle with the electronic subsystem, while the external degrees of freedom act as a storage for mechanical work akin to the flywheel of a macroscopic engine. In this article, we take a first step towards exploring this idea. Using a minimal model consisting of two harmonically trapped Rydberg ions, whose realization was recently reported in Ref. [49], we show that usable work in the form of electronic excitations can be transferred to a vibrational degree of freedom, which forms our flywheel. In lieu of a thermodynamic engine cycle, our device is driven by periodic modulations of the dynamical parameters that control the effective Hamiltonian of the electronic working medium. Our central aim is to demonstrate that Rydberg ion systems, under realistic conditions, provide a potent platform for thermal devices that have access to quantum many-body effects and, at the same time, are capable of delivering significant output to externally accessible work storages.

Model. We consider the setup of Fig. 1. Two Rydberg ions with mass m and charge e are trapped in an isotropic harmonic potential with strength ω. We focus on the longitudinal motion of the ions along their connecting axis, which is governed by the potential $V_{\rm ions}(x_1, x_2) = \frac{1}{2}m\omega^2(x_1^2 + x_2^2) + V_{\rm el}(x_{\rm rel})$. Here, x_k with $k = 1, 2$ are the positions of the ions, $x_{\rm rel} = |x_1 - x_2|$ and $V_{\rm el}(x_{\rm rel}) = e^2/4\pi\epsilon_0 x_{\rm rel}$ denotes the electrostatic potential, where ϵ_0 is the vacuum permittivity [53,54]. At low energies, the ions oscillate around their equilibrium positions x_k^0. The potential $V_{\rm ions}(x_1, x_2)$ can then be expanded to second order in the displacements $\delta x_k = x_k - x_k^0$ [47,55–57]. After separating the center of mass and relative motion and quantizing the relative displacement by making the replacement

$$\delta x_{\rm rel}/\ell_0 = (\delta x_1 - \delta x_2)/\ell_0 \to x = (a^\dagger + a)/\sqrt{2}, \quad (1)$$

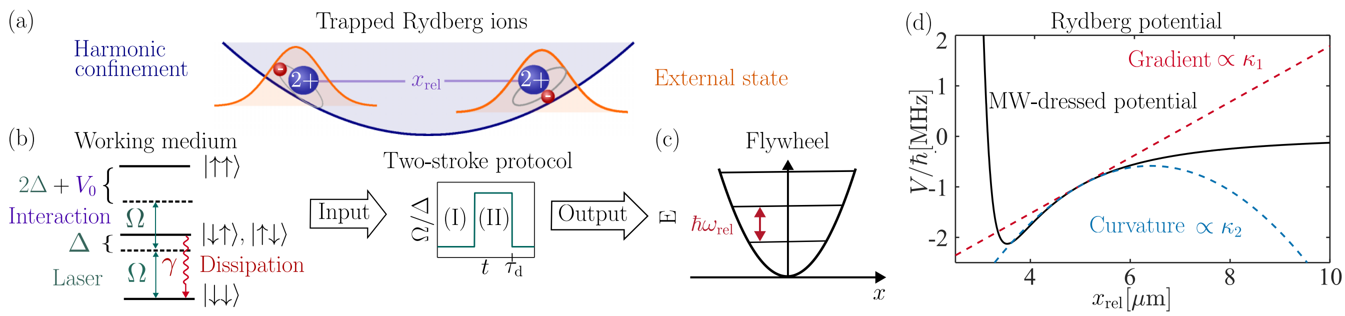

FIG. 1. Rydberg ion flywheel. (a) Setup. Two ions with a doubly charged core and one bound Rydberg electron are confined in a harmonic trap that gives rise to a typical separation of $x_{\rm rel} \simeq 5$ μm. (b) Electronic degrees of freedom (working medium). Each ion is modeled by two electronic states (ground state $|\downarrow\rangle$, Rydberg state $|\uparrow\rangle$). The figure shows the energy-level scheme and transitions associated with the electronic states of two Rydberg ions. A laser drives the transition between ground and Rydberg states with Rabi frequency Ω and detuning Δ; spontaneous decay of the Rydberg states occurs with rate γ. If both ions are excited, the electrostatic interaction among Rydberg states, V_0, shifts the energy of the doubly excited state $|\uparrow\uparrow\rangle$ [50–52], cf. Eq. (2). Cyclically changing Ω or Δ (period $\tau_{\rm d}$) makes it possible to modulate the population of the double excited state periodically and thus the force between the ions. This process excites the vibrational degree of freedom and thereby charges the flywheel. For concreteness, we consider a two-stroke protocol with period $\tau_{\rm d}$, where the control parameter switches between two fixed values. (c) Vibrational degree of freedom (flywheel). At low energies E, the vibrational mode, where the output of the working medium is stored, can be described as a harmonic oscillator with frequency $\omega_{\rm rel}$. (d) Two-ion microwave (MW) dressed potential $V_{\rm int}(x_{\rm rel})$ as a function of the distance $x_{\rm rel}$. Around the ions' equilibrium positions the potential is characterized by its gradient and curvature, which are proportional to the parameters κ_1 and κ_2. The figure is based on the setup of Ref. [46], using dressed Rydberg states of $^{88}{\rm Sr}^+$.

we obtain the Hamiltonian $H_{\rm ph} = \hbar\omega_{\rm rel}(a^\dagger a + 1/2)$ for the vibrational dynamics. Here, $\omega_{\rm rel} = \sqrt{3}\omega$ is the reduced frequency, $\ell_0 = \sqrt{2\hbar/m\omega_{\rm rel}}$ denotes the characteristic length scale of the oscillator, and a and $a^\dagger$ are the usual annihilation and creation operators; for details, see Ref. [58]. The internal degrees of freedom of the ions are modeled as two-level systems with excited Rydberg state $|\uparrow\rangle$ and ground state $|\downarrow\rangle$ [59,60]. The transition between these states is driven by a laser with Rabi frequency Ω and detuning Δ. In the rotating frame of the laser, the free electronic dynamics are described by the Hamiltonian $H_{\rm el} = \hbar\sum_{k=1}^{2}(\Delta n_k + \Omega\sigma_k^x)$, where $\sigma_k^x = |\uparrow_k\rangle\langle\downarrow_k| + |\downarrow_k\rangle\langle\uparrow_k|$ and $n_k = |\uparrow_k\rangle\langle\uparrow_k|$.

When excited to Rydberg states, the ions are subject to the interaction $H_{\rm int} = V_{\rm int}(x_{\rm rel})n_1 n_2$ [59,61,62]. This interaction represents a correction to the potential $V_{\rm ions}$, since its magnitude is small compared with the electrostatic repulsion [63]. This Hamiltonian leads to a shift of the effective energy levels of the ions, see Fig. 1(b), and a state-dependent force that couples their external and internal degrees of freedom. The interaction potential between Rydberg ions is typically of dipolar or van der Waals type [44,53,63,64]. This interaction is, however, generally weaker than that between neutral Rydberg atoms due to a scaling of the electric dipole with the inverse nuclear charge, $Z^{-1} = 1/2$. Strong interactions can nevertheless be realized through microwave (MW) dressing. The gradient and curvature of the resulting potentials can be accurately controlled in experiments [49,53,65], see Fig. 1(d). Upon expanding the such a potential to second order in the relative displacement $\delta x_{\rm rel}$ and quantizing the vibrational degree of freedom as before, we obtain the effective interaction Hamiltonian

$$H_{\rm int} = (V_0 + \hbar\kappa_1 x + \hbar\kappa_2 x^2)n_1 n_2 = \hbar W(x) n_1 n_2. \qquad (2)$$

In this Hamiltonian, $V_0 = V_{\rm int}(x_{\rm rel}^0)$ sets the baseline for the interaction strength, with $x_{\rm rel}^0 = |x_1^0 - x_2^0|$ being the equilibrium distance between the ions; $\hbar\kappa_1 = \ell_0 V'_{\rm int}(x_{\rm rel}^0)$ and $\hbar\kappa_2 = \ell_0^2 V''_{\rm int}(x_{\rm rel}^0)/2$ are proportional to the gradient and the curvature of the potential.

To account for the spontaneous decay of excited Rydberg ions, we complete our model by including a Lindblad-type dissipation superoperator with the form $\mathcal{L}[\bullet] = \gamma\sum_{k=1}^{2}(\sigma_k^- \bullet \sigma_k^+ - \frac{1}{2}\{n_k, \bullet\})$, where $\sigma_k^- = |\downarrow_k\rangle\langle\uparrow_k|$ and $\sigma_k^+ = |\uparrow_k\rangle\langle\downarrow_k|$ are local jump operators, curly brackets denote the anticommutator, and γ is a decay rate, see Fig. 1(b). Hence, the state ϱ of the system follows the quantum master equation

$$\dot\varrho = -\frac{i}{\hbar}[H, \varrho] + \mathcal{L}[\varrho], \qquad (3)$$

with the full Hamiltonian $H = H_{\rm ph} + H_{\rm el} + H_{\rm int}$.

Mean-field dynamics. To explore the dynamics of our model, we proceed with a mean-field approximation, where correlations between internal and external degrees are neglected. The validity of such an approximation is discussed in the Supplemental Material [58], where we compare mean-field results with numerical results obtained by truncating the Fock space. We assume that $\varrho = \varrho_{\rm ph}\otimes\varrho_{\rm el}$, where $\varrho_{\rm ph}$ and $\varrho_{\rm el}$ describe the vibrational and electronic dynamics, respectively. These states follow the mean-field equations

$$\dot\varrho_{\rm ph} = -\frac{i}{\hbar}[\tilde H_{\rm ph}, \varrho_{\rm ph}], \quad \dot\varrho_{\rm el} = -\frac{i}{\hbar}[\tilde H_{\rm el}, \varrho_{\rm el}] + \mathcal{L}[\varrho_{\rm el}], \qquad (4)$$

with $\tilde H_{\rm ph} = H_{\rm ph} + \hbar W(x)s_{nn}$, $\tilde H_{\rm el} = H_{\rm el} + \hbar n_1 n_2\langle W(x)\rangle$. Here, the operator $W(x)$ was defined in Eq. (2) and the variable $s_{nn} = \langle n_1 n_2\rangle$, which corresponds to the population of the double excited state $|\uparrow\uparrow\rangle$, encodes the driven-dissipative dynamics of the electronic subsystem, see Fig. 1(b). Throughout this article, we use the short-hand notation $\langle\bullet\rangle = {\rm Tr}[\bullet\varrho_{\rm ph}\otimes\varrho_{\rm el}]$.

In the mean-field picture, the average relative displacement follows the equation of motion

$$\langle \ddot{x} \rangle + \omega_{\rm rel}(\omega_{\rm rel} + \kappa_2 s_{nn})\langle x \rangle = -\omega_{\rm rel}\kappa_1 s_{nn}. \tag{5}$$

This resembles the equation of motion for a driven harmonic oscillator. However, we note that here the variable s_{nn} is time dependent and even depends on the position $\langle x \rangle$ itself; for the complete set of mean-field equations, see Ref. [58]. This observation suggests that, in order to inject maximal power into the flywheel, the driving protocol for the working medium should be chosen such that s_{nn} oscillates with the eigenfrequency $\omega_{\rm ph} = \sqrt{\omega_{\rm rel}(\omega_{\rm rel} + \kappa_2 s_{nn})}$ of the oscillator (5). To meet this condition, we focus on the regime, where $\kappa_2/\omega_{\rm rel} \ll 1$ and $\omega_{\rm ph} \approx \omega_{\rm rel}$ becomes nearly independent of the electronic state variable s_{nn}. This situation can be realized by tuning the MW-dressed potential and the trap strength ω so that the equilibrium distance $x^0_{\rm rel}$ between the ions comes close to the distance $x^*_{\rm rel}$, where the curvature of the interaction potential vanishes [45,46]. For the parameters used in Fig. 1(d), we have $x^*_{\rm rel} \simeq 3.94$ μm for $\omega \simeq 2\pi \times 145$ kHz, which is a realistic value in typical experiments with Rydberg ions [40,41,49]. The baseline interaction strength, the gradient of the interaction potential, the Rydberg state decay rate, and the characteristic length of the vibrational subsystem then become $V_0/\hbar \simeq -1.8$ MHz, $\kappa_1 = \gamma \simeq 0.1$ MHz, and $\ell_0 \simeq 0.1$ μm. In the following analysis, we use these values as a reference.

Results. To charge our flywheel, we vary either the Rabi frequency Ω or the detuning Δ of the laser according to the periodic two-stroke protocol shown in Fig. 1(b); the switching occurs at $t = \tau_{\rm d}/2$ and the period is set to $\tau_{\rm d} = 2\pi/\omega_{\rm rel}$; the detuning can be controlled, for instance, through external fields affecting the energy levels of the ions. The level scheme in Fig. 1(b) shows that the alignment between the effective energy levels of the working medium and the transitions driven by the laser depends on both Ω and Δ. As a result, both parameters affect the rate at which excitations are created in the electronic system and can therefore be used to imprint a periodic modulation on the double-excitation probability s_{nn}, which controls the repulsion force between the ions. This mechanism enables a continuous transfer of energy from the working medium to the flywheel, which leads to the gradual increase of its oscillation amplitude seen in Fig. 2. In line with our physical picture, the charging process is suppressed, and even reversed, at long times for $\kappa_2 \neq 0$, as the flywheel is shifted out of resonance with the driving. We note that the runtime of the flywheel is limited since the width of the ion wave-packages must be much smaller than their equilibrium distance to ensure the validity of the approximated interaction potential. For the parameters used in Fig. 2, this condition is met for $t \leqslant 400/\gamma$. In experiments also the phononic modes experience some dissipation. However, as we show in the Supplemental Material [58], parameter regimes can be identified in which this is negligible.

The qualitative behavior of the mean distance $\langle x \rangle$ can be further understood from the high-frequency limit. To this end, we first observe that the mean-field equations (4) decouple for $\kappa_1 = \kappa_2 = 0$. After some relaxation time τ_0, which is essentially determined by γ, the electronic state $\varrho_{\rm el}$ then settles

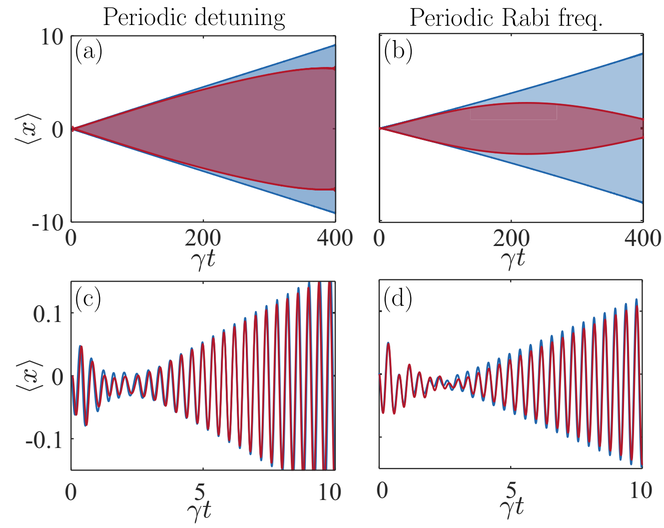

FIG. 2. Charging the flywheel. (a) Average distance between the Rydberg ions in units of ℓ_0 as a function of time for two different values of the curvature parameter κ_2; the detuning Δ switches cyclically between $\Delta_{\rm min} = 0$ and $\Delta_{\rm max} = 9\gamma$, while the Rabi frequency $\Omega = 8\gamma$ is fixed. (b) Same plot as in panel (a) with Ω switching between $\Omega_{\rm min} = 2\gamma$ and $\Omega_{\rm max} = 8\gamma$ and $\Delta = 9\gamma$ fixed. The blue curves were obtained with $V_0 = -18\hbar\gamma$ and $\kappa_2 = 0$; the red ones with $V_0 = -17\hbar\gamma$ and $\kappa_2 = -0.1\gamma$. Panels (c) and (d) show the oscillatory short-time dynamics of the flywheel. For all plots, we have chosen $\omega = 9\gamma$, $\kappa_1 = \gamma$ and initially set $\varrho_{\rm ph} = |0\rangle\langle 0|$ and $\varrho_{\rm el} = |{\downarrow\downarrow}\rangle\langle{\downarrow\downarrow}|$, where $|0\rangle$ is the ground state of the oscillator.

to a unique limit cycle, which satisfies $\varrho^{\rm lc}_{\rm el}(t) = \varrho^{\rm lc}_{\rm el}(t + \tau_{\rm d})$.[1] Hence, s_{nn} acquires the same periodicity as the driving. For $0 < |\kappa_1| \ll \omega_{\rm rel}$, the oscillator (5) is affected by driving only over a large number of periods. Thus, $\langle x \rangle$ remains $\tau_{\rm d}$ periodic on short timescales and develops modulations on some longer scale $\tau_{\rm mod} = 1/\epsilon$. That is, $\langle x \rangle = \langle x \rangle(\epsilon t, \omega_{\rm rel} t)$ can be written as a Fourier series with slowly drifting coefficients,

$$\langle x \rangle = \sum_{n\in\mathbb{Z}} c_n(\epsilon t)e^{in\omega_{\rm rel}t} = \epsilon t \langle x \rangle_1(\omega_{\rm rel}t) + O(\epsilon^2). \tag{6}$$

Here, we have expanded in ϵ and used $\langle x \rangle = \langle \dot{x} \rangle = 0$ at $t = 0$ so that $\langle x \rangle \to 0$ for $\epsilon \to 0$; note that we understand any function of $\omega_{\rm rel}t$ to be 2π periodic in this argument. The time-dependence of $\langle x \rangle$ now carries over to the mean-field Hamiltonian $\tilde{H}_{\rm el}$, which is thus no longer strictly periodic. However, if $\epsilon\tau_0 \ll 1$, the working medium still follows its instantaneous limit-cycle on the long timescale. Thus, we have $\varrho_{\rm el} \approx \varrho^{\rm lc}_{\rm el}(\epsilon t, \omega_{\rm rel}t)$ and $s_{nn} \approx s_{nn}(\epsilon t, \omega_{\rm rel}t) = \frac{1}{2}\sum_{n\in\mathbb{Z}} d_n(\epsilon t)e^{in\omega_{\rm rel}t}$ for $t > \tau_0$. The scale of the modulation rate ϵ can now be determined self-consistently. Inserting the ansatz $\langle x \rangle = \langle x \rangle(\epsilon t, \omega_{\rm rel}t)$ into Eq. (5) and setting $\kappa_2 = 0$

[1]This statement follows from the observation that the Lindblad generator $\mathcal{L}$ in Eq. (4) has only one eigenvalue with vanishing real part as can be easily confirmed by inspection; for further details see Ref. [66].

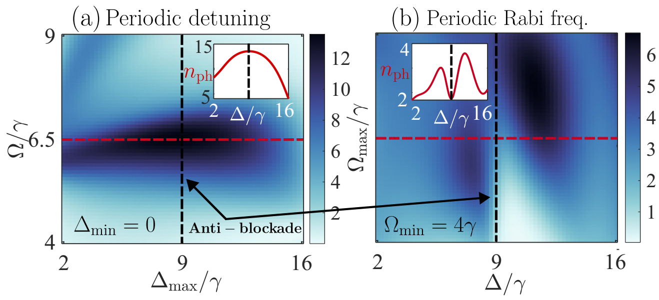

FIG. 3. Energy of the flywheel. The plots show the average excitation number $n_{\rm ph}$ after a runtime of $t = 100/\gamma$ for both driving modes as a function of (a) the Rabi frequency and the maximal detuning and (b) the maximal Rabi frequency and the fixed detuning. The insets show cuts through the density plots along the horizontal dashed lines. The vertical dashed lines indicate the antiblockade condition, see main text for details. For all plots, we have chosen the parameters $\omega = 9\gamma$, $V_0 = -18\hbar\gamma$, $\kappa_1 = \gamma$, and $\kappa_2 = 0$.

gives

$$\begin{aligned}\langle x\rangle &= -\kappa_1 \int_0^t dt' |d_1(\epsilon t')| \cos\left[\omega_{\rm rel} t + \varphi_1(\epsilon t')\right] + O(\kappa_1/\omega_{\rm rel})\\ &= -\kappa_1 |d_1(0)| t \cos\left[\omega_{\rm rel} t + \varphi_1(0)\right] + O(\kappa_1/\omega_{\rm rel}, \epsilon),\end{aligned}$$

where φ_1 is a phase shift. Comparing this results with Eq. (6) shows that ϵ must be of the same order of magnitude as $|\kappa_1 d_1(0)|$. Finally, for $\gamma \ll \omega_{\rm rel}$, the electronic system is barely able to follow the driving protocol and the unperturbed oscillation amplitude $d_1(0)$ of s_{nn} is of order $\gamma/\omega_{\rm rel}$. We then have $\epsilon\tau_0 \sim \epsilon/\gamma \sim |\kappa_1|/\omega_{\rm rel} \ll 1$, which shows that our estimate is self-consistent in the high-frequency regime.

The above argument still holds for $\kappa_2 \neq 0$ as long as $|\kappa_2|/\omega_{\rm rel} \ll 1$. Quite intuitively, it shows that the charging rate ϵ of our flywheel is essentially determined by the strength of its interaction with the working medium and frequency of the external harmonic trap, $\omega = \omega_{\rm rel}/\sqrt{3}$. However, the specific choice of the driving protocol does not play a dominant role. We note that the estimate $\epsilon \sim \gamma|\kappa_1|/\omega_{\rm rel}$ is also in good agreement with our numerical simulations; for the parameters chosen in Fig. 2, the charging rate is $\epsilon \approx \gamma/40$, while $\gamma|\kappa_1|/\omega_{\rm rel} \approx \gamma/16$.

To further explore the phenomenology of our model, we now analyze the energy content of our flywheel, which is proportional to the mean excitation number $n_{\rm ph} = \langle a^\dagger a\rangle$. This quantity is plotted in Fig. 3 as a function of the laser parameters for both driving modes and a runtime of $t = 100/\gamma$. The main features of these plots can be understood as follows:

For periodically changing detuning, we observe a pronounced maximum when $\Delta_{\max}$ meets the so-called antiblockade condition $2\Delta + V_0/\hbar = 0$ [67–71]. The transition between ground and double excited state of the working medium is then resonant with the laser during the second stroke of the protocol, which leads to a strong increase of s_{nn}, see Fig. 1(c). Leaving the antiblockade regime in the first stroke by changing the detuning so that $\Delta \ll \Delta_{\max}$ leads to a sharp decay in the double excitation probability due to spontaneous decay. As a result, s_{nn} develops a large oscillation amplitude, which gives rise to a large charging rate.

By contrast, if the system is driven through the Rabi frequency of the laser, the antiblockade regime features a dip in the energy of the flywheel. This observation can be explained by considering the three relevant eigenstates, $|\downarrow\downarrow\rangle$, $|\uparrow\uparrow\rangle$, and $|S\rangle \propto |\downarrow\uparrow\rangle + |\uparrow\downarrow\rangle$, of the reduced mean-field Hamiltonian $\tilde{H}_{\rm el}^0 = \hbar\Delta\sum_{k=1}^2 n_k + V_0 n_1 n_2$; the antisymmetric superposition of the single excited states does not couple to the laser due to the permutation symmetry of $\tilde{H}_{\rm el}$. If the antiblockade condition is met, the state $|\downarrow\downarrow\rangle$ and the state $|\uparrow\uparrow\rangle$ are both ground states of the Hamiltonian $\tilde{H}_{\rm el}^0$. The superpositions $|D\rangle \propto |\downarrow\downarrow\rangle - |\uparrow\uparrow\rangle$ and $|B\rangle \propto |\downarrow\downarrow\rangle + |\uparrow\uparrow\rangle$ then correspond to a dark and a bright state of the system, respectively [72]. Since neither of these states depends on Ω, the dark state becomes a stable fixed point of the dynamics, in which the working medium is effectively trapped; note that such a fixed point does not exist if the antiblockade condition is periodically lifted by changing the detuning and the emergence of this dark-state has no classical counterpart. This mechanism suppresses the oscillation amplitude of s_{nn}, and thus the charging rate. We note that the above argument, although covering the dominant physical process, does not account for spontaneous decay or the modulation of the electronic Hamiltonian through the position of the flywheel. Therefore, we still expect the charging rate to remain finite if the antiblockade condition is met, as our simulations show.

Concluding perspectives. In this work, we have analyzed a minimal yet realistic model of an integrated thermal machine based on laser-driven Rydberg ions. The electronic degrees of freedom of the ions provide a working medium for a thermodynamic cycle, here mimicked through periodic variations of external control parameters. Their translational degrees of freedom, on the other hand, act as a flywheel storing the generated work output. To what extent this output is accessible to secondary devices will depend on the specifics of the coupling mechanism. If arbitrary unitary transformations can be applied to extract work from the flywheel, the maximal accessible energy is given by its *ergotropy* [73], which, in the mean-field regime, is, up to a constant shift [74], equivalent to the internal energy plotted in Fig. 3.

Our study demonstrates that Rydberg-ion systems are a viable experimental platform for microscopic thermal devices that feature genuine quantum effects and are capable of delivering output to an external storage system. Furthermore, our model can, in principle, be scaled up to a many-body device by replacing the pair of ions with an ionic Wigner crystal [75–77], where selected phonon modes play the role of the flywheel. This step, which promises to reveal a rich phenomenology arising from many-body effects, along with a complete thermodynamic analysis of our model and the integration of proper thermodynamic cycles driven by thermal rather than coherent energy sources rather are left to future research. Our results here provide both a well-defined starting point and a valuable benchmark for these investigations.

Acknowledgments. We acknowledge funding from the Deutsche Forschungsgemeinschaft (DFG, German Research Foundation) through the Research Unit FOR 5413/1, Grant No. 465199066. This project has also received funding from the European Union's Horizon Europe research and innovation program under Grant Agreement No. 101046968 (BRISQ). F.C. is indebted to the Baden-Württemberg Stiftung for the financial support by the Eliteprogramme for Postdocs.

This work was supported by the University of Nottingham and the University of Tübingen's funding as part of the Excellence Strategy of the German Federal and State Governments, in close collaboration with the University of Nottingham. K.B. acknowledges support from the University of Nottingham through a Nottingham Research Fellowship. This work was supported by the Medical Research Council [Grant No. MR/S034714/1]; and the Engineering and Physical Sciences Research Council [Grants No. EP/V031201/1 and No. EP/W015641/1].

[1] U. Seifert, Stochastic thermodynamics, fluctuation theorems and molecular machines, Rep. Prog. Phys. **75**, 126001 (2012).
[2] R. Kosloff, Quantum thermodynamics: A dynamical viewpoint, Entropy **15**, 2100 (2013).
[3] S. Vinjanampathy and J. Anders, Quantum thermodynamics, Contemp. Phys. **57**, 545 (2016).
[4] G. Benenti, G. Casati, K. Saito, and R. Whitney, Fundamental aspects of steady-state conversion of heat to work at the nanoscale, Phys. Rep. **694**, 1 (2017).
[5] A. S. Trushechkin, M. Merkli, J. D. Cresser, and J. Anders, Open quantum system dynamics and the mean force Gibbs state, AVS Quantum Sci. **4**, 012301 (2022).
[6] L. Arrachea, Energy dynamics, heat production and heat–work conversion with qubits: Toward the development of quantum machines, Rep. Prog. Phys. **86**, 036501 (2023).
[7] J. Roßnagel, S. T. Dawkins, K. N. Tolazzi, O. Abah, E. Lutz, F. Schmidt-Kaler, and K. Singer, A single-atom heat engine, Science **352**, 325 (2016).
[8] D. von Lindenfels, O. Gräb, C. T. Schmiegelow, V. Kaushal, J. Schulz, M. T. Mitchison, J. Goold, F. Schmidt-Kaler, and U. G. Poschinger, Spin heat engine coupled to a harmonic-oscillator flywheel, Phys. Rev. Lett. **123**, 080602 (2019).
[9] N. V. Horne, D. Yum, T. Dutta, P. Hänggi, J. Gong, D. Poletti, and M. Mukherjee, Single-atom energy-conversion device with a quantum load, npj Quantum Inf. **6**, 37 (2020).
[10] J. P. S. Peterson, T. B. Batalhão, M. Herrera, A. M. Souza, R. S. Sarthour, I. S. Oliveira, and R. M. Serra, Experimental characterization of a spin quantum heat engine, Phys. Rev. Lett. **123**, 240601 (2019).
[11] J. Klatzow, J. N. Becker, P. M. Ledingham, C. Weinzetl, K. T. Kaczmarek, D. J. Saunders, J. Nunn, I. A. Walmsley, R. Uzdin, and E. Poem, Experimental demonstration of quantum effects in the operation of microscopic heat engines, Phys. Rev. Lett. **122**, 110601 (2019).
[12] Q. Bouton, J. Nettersheim, S. Burgardt, D. Adam, E. Lutz, and A. Widera, A quantum heat engine driven by atomic collisions, Nat. Commun. **12**, 2063 (2021).
[13] V. Mukherjee and U. Divakaran, Many-body quantum thermal machines, J. Phys.: Condens. Matter **33**, 454001 (2021).
[14] A. Ü. C. Hardal and Ö. E. Müstecaplıoğlu, Superradiant quantum heat engine, Sci. Rep. **5**, 12953 (2015).
[15] R. Uzdin, Coherence-induced reversibility and collective operation of quantum heat machines via coherence recycling, Phys. Rev. Appl. **6**, 024004 (2016).
[16] W. Niedenzu and G. Kurizki, Cooperative many-body enhancement of quantum thermal machine power, New J. Phys. **20**, 113038 (2018).
[17] C. L. Latune, I. Sinayskiy, and F. Petruccione, Thermodynamics from indistinguishability: Mitigating and amplifying the effects of the bath, Phys. Rev. Res. **1**, 033192 (2019).
[18] C. L. Latune, I. Sinayskiy, and F. Petruccione, Collective heat capacity for quantum thermometry and quantum engine enhancements, New J. Phys. **22**, 083049 (2020).
[19] H. Tajima and K. Funo, Superconducting-like heat current: Effective cancellation of current-dissipation trade-off by quantum coherence, Phys. Rev. Lett. **127**, 190604 (2021).
[20] S. Kamimura, H. Hakoshima, Y. Matsuzaki, K. Yoshida, and Y. Tokura, Quantum-enhanced heat engine based on superabsorption, Phys. Rev. Lett. **128**, 180602 (2022).
[21] L. da Silva Souza, G. Manzano, R. Fazio, and F. Iemini, Collective effects on the performance and stability of quantum heat engines, Phys. Rev. E **106**, 014143 (2022).
[22] M. A. Macovei, Performance of the collective three-level quantum thermal engine, Phys. Rev. A **105**, 043708 (2022).
[23] J. Kim, S.-h. Oh, D. Yang, J. Kim, M. Lee, and K. An, A photonic quantum engine driven by superradiance, Nat. Photon. **16**, 707 (2022).
[24] D. Kolisnyk and G. Schaller, Performance boost of a collective qutrit refrigerator, Phys. Rev. Appl. **19**, 034023 (2023).
[25] J. Jaramillo, M. Beau, and A. del Campo, Quantum supremacy of many-particle thermal machines, New J. Phys. **18**, 075019 (2016).
[26] J. Li, T. Fogarty, S. Campbell, X. Chen, and T. Busch, An efficient nonlinear Feshbach engine, New J. Phys. **20**, 015005 (2018).
[27] Y.-Y. Chen, G. Watanabe, Y.-C. Yu, X.-W. Guan, and A. del Campo, An interaction-driven many-particle quantum heat engine and its universal behavior, npj Quantum Inf. **5**, 88 (2019).
[28] N. M. Myers and S. Deffner, Bosons outperform fermions: The thermodynamic advantage of symmetry, Phys. Rev. E **101**, 012110 (2020).
[29] T. Fogarty and T. Busch, A many-body heat engine at criticality, Quantum Sci. Technol. **6**, 015003 (2021).
[30] T. Keller, T. Fogarty, J. Li, and T. Busch, Feshbach engine in the Thomas-Fermi regime, Phys. Rev. Res. **2**, 033335 (2020).
[31] G. Watanabe, B. P. Venkatesh, P. Talkner, M.-J. Hwang, and A. del Campo, Quantum statistical enhancement of the collective performance of multiple bosonic engines, Phys. Rev. Lett. **124**, 210603 (2020).
[32] N. M. Myers, J. McCready, and S. Deffner, Quantum heat engines with singular interactions, Symmetry **13**, 978 (2021).
[33] N. M. Myers, F. J. Peña, O. Negrete, P. Vargas, G. D. Chiara, and S. Deffner, Boosting engine performance with Bose-Einstein condensation, New J. Phys. **24**, 025001 (2022).
[34] J. Eglinton, T. Pyharanta, K. Saito, and K. Brandner, Thermodynamic geometry of ideal quantum gases: A general framework and a geometric picture of BEC-enhanced heat engines, New J. Phys. **25**, 043014 (2023).

[35] J. Koch, K. Menon, E. Cuestas, S. Barbosa, E. Lutz, T. Fogarty, T. Busch, and A. Widera, A quantum engine in the BEC-BCS crossover, Nature (London) **621**, 723 (2023).
[36] K. Zhang, F. Bariani, and P. Meystre, Quantum optomechanical heat engine, Phys. Rev. Lett. **112**, 150602 (2014).
[37] F. Carollo, K. Brandner, and I. Lesanovsky, Nonequilibrium many-body quantum engine driven by time-translation symmetry breaking, Phys. Rev. Lett. **125**, 240602 (2020).
[38] J. Sheng, C. Yang, and H. Wu, Realization of a coupled-mode heat engine with cavity-mediated nanoresonators, Sci. Adv. **7**, eabl7740 (2021).
[39] F. Carollo, F. M. Gambetta, K. Brandner, J. P. Garrahan, and I. Lesanovsky, Nonequilibrium quantum many-body Rydberg atom engine, Phys. Rev. Lett. **124**, 170602 (2020).
[40] G. Higgins, W. Li, F. Pokorny, C. Zhang, F. Kress, C. Maier, J. Haag, Q. Bodart, I. Lesanovsky, and M. Hennrich, Single strontium Rydberg ion confined in a Paul trap, Phys. Rev. X **7**, 021038 (2017).
[41] G. Higgins, F. Pokorny, C. Zhang, Q. Bodart, and M. Hennrich, Coherent control of a single trapped Rydberg ion, Phys. Rev. Lett. **119**, 220501 (2017).
[42] A. Mokhberi, M. Hennrich, and F. Schmidt-Kaler, Trapped Rydberg ions: A new platform for quantum information processing, Adv. At. Mol. Opt. Phys. **69**, 233 (2020).
[43] W. Li and I. Lesanovsky, Electronically excited cold ion crystals, Phys. Rev. Lett. **108**, 023003 (2012).
[44] F. M. Gambetta, I. Lesanovsky, and W. Li, Exploring nonequilibrium phases of the generalized Dicke model with a trapped Rydberg-ion quantum simulator, Phys. Rev. A **100**, 022513 (2019).
[45] F. M. Gambetta, W. Li, F. Schmidt-Kaler, and I. Lesanovsky, Engineering nonbinary Rydberg interactions via phonons in an optical lattice, Phys. Rev. Lett. **124**, 043402 (2020).
[46] F. M. Gambetta, C. Zhang, M. Hennrich, I. Lesanovsky, and W. Li, Long-range multibody interactions and three-body antiblockade in a trapped Rydberg ion chain, Phys. Rev. Lett. **125**, 133602 (2020).
[47] F. M. Gambetta, C. Zhang, M. Hennrich, I. Lesanovsky, and W. Li, Exploring the many-body dynamics near a conical intersection with trapped Rydberg ions, Phys. Rev. Lett. **126**, 233404 (2021).
[48] M. Magoni, R. Joshi, and I. Lesanovsky, Molecular dynamics in Rydberg tweezer arrays: Spin-phonon entanglement and Jahn-Teller effect, Phys. Rev. Lett. **131**, 093002 (2023).
[49] C. Zhang, F. Pokorny, W. Li, G. Higgins, A. Pöschl, I. Lesanovsky, and M. Hennrich, Submicrosecond entangling gate between trapped ions via Rydberg interaction, Nature (London) **580**, 345 (2020).
[50] M. D. Lukin, M. Fleischhauer, R. Cote, L. M. Duan, D. Jaksch, J. I. Cirac, and P. Zoller, Dipole blockade and quantum information processing in mesoscopic atomic ensembles, Phys. Rev. Lett. **87**, 037901 (2001).
[51] E. Urban, T. A. Johnson, T. Henage, L. Isenhower, D. D. Yavuz, T. G. Walker, and M. Saffman, Observation of Rydberg blockade between two atoms, Nat. Phys. **5**, 110 (2009).
[52] D. Comparat and P. Pillet, Dipole blockade in a cold Rydberg atomic sample, J. Opt. Soc. Am. B **27**, A208 (2010).
[53] M. Müller, L. Liang, I. Lesanovsky, and P. Zoller, Trapped Rydberg ions: From spin chains to fast quantum gates, New J. Phys. **10**, 093009 (2008).
[54] F. Schmidt-Kaler, T. Feldker, D. Kolbe, J. Walz, M. Müller, P. Zoller, W. Li, and I. Lesanovsky, Rydberg excitation of trapped cold ions: A detailed case study, New J. Phys. **13**, 075014 (2011).
[55] H. Labuhn, D. Barredo, S. Ravets, S. de Léséleuc, T. Macrì, T. Lahaye, and A. Browaeys, Tunable two-dimensional arrays of single Rydberg atoms for realizing quantum Ising models, Nature (London) **534**, 667 (2016).
[56] M. Endres, H. Bernien, A. Keesling, H. Levine, E. R. Anschuetz, A. Krajenbrink, C. Senko, V. Vuletic, M. Greiner, and M. D. Lukin, Atom-by-atom assembly of defect-free one-dimensional cold atom arrays, Science **354**, 1024 (2016).
[57] V. Lienhard, S. de Léséleuc, D. Barredo, T. Lahaye, A. Browaeys, M. Schuler, L.-P. Henry, and A. M. Läuchli, Observing the space- and time-dependent growth of correlations in dynamically tuned synthetic Ising models with antiferromagnetic interactions, Phys. Rev. X **8**, 021070 (2018).
[58] See Supplemental Material at http://link.aps.org/supplemental/10.1103/PhysRevA.108.L050201 for details of the calculation and additional simulation results.
[59] R. Löw, H. Weimer, J. Nipper, J. B. Balewski, B. Butscher, H. P. Büchler, and T. Pfau, An experimental and theoretical guide to strongly interacting Rydberg gases, J. Phys. B: At., Mol. Opt. Phys. **45**, 113001 (2012).
[60] M. Marcuzzi, J. Minář, D. Barredo, S. de Léséleuc, H. Labuhn, T. Lahaye, A. Browaeys, E. Levi, and I. Lesanovsky, Facilitation dynamics and localization phenomena in Rydberg lattice gases with position disorder, Phys. Rev. Lett. **118**, 063606 (2017).
[61] T. F. Gallagher, Rydberg atoms, Rep. Prog. Phys. **51**, 143 (1988).
[62] A. Browaeys, D. Barredo, and T. Lahaye, Experimental investigations of dipole-dipole interactions between a few Rydberg atoms, J. Phys. B: At., Mol. Opt. Phys. **49**, 152001 (2016).
[63] M. Saffman, T. G. Walker, and K. Mølmer, Quantum information with Rydberg atoms, Rev. Mod. Phys. **82**, 2313 (2010).
[64] T. G. Walker and M. Saffman, Consequences of Zeeman degeneracy for the van der Waals blockade between Rydberg atoms, Phys. Rev. A **77**, 032723 (2008).
[65] J. Vogel, W. Li, A. Mokhberi, I. Lesanovsky, and F. Schmidt-Kaler, Shuttling of Rydberg ions for fast entangling operations, Phys. Rev. Lett. **123**, 153603 (2019).
[66] P. Menczel and K. Brandner, Limit cycles in periodically driven open quantum systems, J. Phys. A: Math. Theor. **52**, 43LT01 (2019).
[67] C. Ates, T. Pohl, T. Pattard, and J. M. Rost, Antiblockade in Rydberg excitation of an ultracold lattice gas, Phys. Rev. Lett. **98**, 023002 (2007).
[68] T. Amthor, C. Giese, C. S. Hofmann, and M. Weidemüller, Evidence of antiblockade in an ultracold Rydberg gas, Phys. Rev. Lett. **104**, 013001 (2010).
[69] J. T. Young, T. Boulier, E. Magnan, E. A. Goldschmidt, R. M. Wilson, S. L. Rolston, J. V. Porto, and A. V. Gorshkov, Dissipation-induced dipole blockade and antiblockade in driven Rydberg systems, Phys. Rev. A **97**, 023424 (2018).
[70] L. Festa, N. Lorenz, L.-M. Steinert, Z. Chen, P. Osterholz, R. Eberhard, and C. Gross, Blackbody-radiation-induced facilitated excitation of Rydberg atoms in optical tweezers, Phys. Rev. A **105**, 013109 (2022).

[71] M. Magoni, P. P. Mazza, and I. Lesanovsky, Phonon dressing of a facilitated one-dimensional Rydberg lattice gas, SciPost Phys. Core **5**, 041 (2022).

[72] D. D. B. Rao and K. Mølmer, Dark entangled steady states of interacting Rydberg atoms, Phys. Rev. Lett. **111**, 033606 (2013).

[73] A. E. Allahverdyan, R. Balian, and T. M. Nieuwenhuizen, Maximal work extraction from finite quantum systems, Europhys. Lett. **67**, 565 (2004).

[74] The ergotropy is defined by $\mathcal{E} = \mathrm{tr}[\varrho_t H] - \min_U \mathrm{tr}[HU\varrho U^\dagger]$, with $U^\dagger U = \mathbb{1}$. In the present system, for an initial phononic state $|0\rangle\langle 0|$ it reduces to $\mathcal{E} = \mathrm{tr}[H_{\mathrm{ph}}\varrho_{\mathrm{ph}}] - \langle 0|H_{\mathrm{ph}}|0\rangle = \mathrm{tr}[H_{\mathrm{ph}}\varrho_{\mathrm{ph}}] - \hbar\omega_{\mathrm{rel}}/2$.

[75] D. James, Quantum dynamics of cold trapped ions with application to quantum computation, Appl. Phys. B: Lasers Opt. **66**, 181 (1998).

[76] D. Porras and J. I. Cirac, Effective quantum spin systems with trapped ions, Phys. Rev. Lett. **92**, 207901 (2004).

[77] X.-L. Deng, D. Porras, and J. I. Cirac, Effective spin quantum phases in systems of trapped ions, Phys. Rev. A **72**, 063407 (2005).